Article

Visible Light–Near-Infrared Photodetection on Cys-MoO$_{3-x}$ Nanoparticles for Photothermal Therapy against Papillary Thyroid Carcinoma

Jinhuan Chen [1,2], Xian Liu [1], Xin Zeng [2], Ming Yang [3,*] and Liang Xie [2,*]

1 Emergency Department, West China Hospital of Stomatology, Sichuan University, Chengdu 610041, China; chenjinhuan32@scu.edu.cn (J.C.)
2 State Key Laboratory of Oral Diseases, National Center for Stomatology, National Clinical Research Center for Oral Diseases, Research Unit of Oral Carcinogenesis and Management, Chinese Academy of Medical Sciences, West China Hospital of Stomatology, Sichuan University, Chengdu 610041, China
3 Institute of Electronic and Electrical Engineering, Civil Aviation Flight University of China, No. 46 Section 4, Nanchang Road, Guanghan 618307, China
* Correspondence: yangming932@cafuc.edu.cn (M.Y.); lxie@scu.edu.cn (L.X.)

Abstract: The excellent performance of semiconductor nanocrystals as sensitizers for photothermal therapy (PTT) has attracted the attention of many researchers; however, they are hindered by limited bandwidth and complex synthesis. To overcome these limitations, starting with an initial determination of photothermal conductivity, we synthesized and designed molybdenum and Cys-MoO$_{3-x}$ nanoparticles (NPs) for use in the minimally invasive treatment of papillary thyroid carcinoma (PTC), as the NPs are coated only with cysteine molecules. The obtained Cys-MoO$_2$ NPs were used as a PTT reaction drug for topical application to PTC cells. The use of near-infrared photoconductive PTT in combination with low-toxicity biological chemotherapy reached a 90% efficacy for cancer treatment in vitro. The conducted experiments intuitively demonstrate that non-toxic Cys-MoO$_2$ NPs are lethal to the cancer cells under visual (VL, 405 nm) and near-infrared (NIR, 808 nm) laser irradiation and can be precisely controlled. Therefore, this study provides a powerful, safe, and easily modified NP platform for photo-triggered PTC elimination with broad application prospects. Assessment of the ideal damage range indicates a high degree of controllability, allowing the tumor to be precisely targeted while minimizing damage to the surrounding healthy tissue. In conclusion, this study provides a convenient, safe, and powerful NP platform for the near-infrared photo-controlled PTT of PTC cells, which has broad application prospects for the elimination of PTC and other types of cancer.

Keywords: photothermal therapy (PTT); papillary thyroid carcinoma; photodetection; nanoparticles; NIR laser

1. Introduction

Thyroid cancer is a high-incidence malignant endocrine tumor in the field of head and neck cancer [1–3], regarding which, papillary thyroid carcinoma (PTC) is the most common thyroid malignancy [4]. The incidence of PTC has been reported to be continuously increasing, due to the popularization of cancer screening, over the last few decades [5]. Even though surgery remains the standard treatment, it may be associated with complications [6]. Therefore, modern medicine for the management of PTCs has developed toward non-surgical and minimally invasive treatment strategies [7,8]. Photothermal therapy (PTT)—a new minimally invasive technique for cancer treatment—is being applied in wider and wider scopes, and has already been utilized as a complementary therapy for conventional surgical excision procedures in a clinical trial on cancer [9]. As a novel therapy with various different mechanisms of action, PTT is likely necessary to achieve a significant improvement in the fight against PTCs [10,11].

Generally, PTT involves a treatment that achieves the artificial temperature elevation of optically sensitive agents in local tissue, triggering hyperthermia or thermal ablation to eliminate cancer cells [12]. It makes use of the intolerance of target cells to heat, resulting in apoptosis or necrosis. Due to the high penetration efficiency of near-infrared (NIR) light through the human body, NIR light is typically selected as the excitation light [13–15]. Thus, the NIR absorption capabilities of a range of PTT reagents, such as metal nanoparticles (NPs) [16,17], carbon-based nanomaterials [18,19], organic dyes and polymers [20,21], and semiconductors [22,23], has recently been reported. Despite the developments made to date, the balance between the high efficiency of PTT—which requires high-penetration lasers to effectively stimulate tumor cell death—and a low risk of radiation damage to adjacent normal tissues is not easy to achieve. Structurally flawless nanocrystals may inherit crucial defects through both in vivo biodegradation and in vitro physiological environment decomposition [24–26]. Therefore, considering promising transition metal oxides, molybdenum oxide nanomaterials have gradually come into focus as photothermal therapy agents (PTAs) with high potential in recent years [27,28]. Not only can a variety of Mo-reduced-valence (MoO_{3-x}) species be derived, which vary in terms of morphology, structure, and properties, but MoO_{3-x} NPs also present high biological safety, an ease of excretion, and a high light absorption efficiency in both the visible and near-infrared regions, due to their unique defect structure [29–33].

As simple MoO_2 and MoO_3 crystals have good conductivity but do not present localized surface plasmon resonance, their structures must be improved or modified with other substances; however, instability, strict preparation environment requirements, and large synthetic energy demands limit the production of modified MoO_{3-x} [34,35]. Besides PTT efficiency, significant attention must be paid to the biosafety of photothermal agents [36]. In a previous study, we improved the uptake of NPs into tumor cells by the reduction in Mo through the use of cysteine, and took full advantage of the enhanced permeability and retention (EPR) effect through the optimization of the size of the NPs [37–40]. These MoO_{3-x} NPs were shown to be effective and bio-safe with respect to certain kinds of tumor cells [41]. Hence, starting with an optical performance evaluation of MoO_{3-x} as the core with a cysteine coating, we further optimized the single-component Cys-MoO_2 NP products for application through an in vitro experiment involving papillary thyroid carcinoma cells. We conducted multiple validations to prove their biosafety, and they obtained lethality rates for PTC cells over 90% and 45% under NIR 808 nm and VL 405 nm lasers, respectively. Through further in vivo experiments, we further verified the biosafety and therapeutic effect of the designed NPs. In summary, in this paper, we detail the synthesis of a newly reported material, Cys-MoO_2, as well as the screening of its optical properties, photo-thermal conductivity, biosafety, and in vitro application specific to PTC cells, in order to verify its photothermal efficiency and move toward more effective PTT against PTCs as a minimally invasive therapeutic approach.

2. Materials and Methods

2.1. Materials Preparation

Molybdenum sulfide, L-cysteine (Sigma Aldrich, St. Louis, MO, USA) and H_2O_2 (Jin Shan Chemical Test) were obtained. PTC cells (B-CPAP) were obtained from the Key Laboratory of Stem Cell Biology Shanghai Institutes for Biological Sciences at the Chinese Academy of Sciences. First, 80 mg of pristine MoS_2 powder and 3.75 mL 30 wt% H_2O_2 were gradually mixed into 46.25 mL deionized water, then stirred until all solid reagents had completely dissolved. Then, the produced brown-yellow solution was heated to eliminate unreacted H_2O_2. Then, various amounts of cysteine (5 mg, 10 mg, 20 mg, 40 mg, or 80 mg) were added into 1.5 mL of the obtained solution to yield MoO_3 in different reductant valence states (Mo molality: 10×10^{-3} M).

2.2. Structural and Optical Characteristics

We conducted XPS spectrometry (Bruker AXS D8 Advance) to calculate the specific Mo content in the obtained Cys-MoO$_{3-x}$ solutions. Then, the two optimized compounds were tested using transmission electron microscopy (JEOL, Akishima, Japan) to examine their morphologies, as well as spectrophotometry (Thermo Variskan LUX, Waltham, MA, USA) to detect their absorption spectra. A Keithley 2636B instrument was used to test the I$_{ph}$ of different Cys-MoO$_2$ NPs at normal temperatures and pressures. A Malvern Zetasizer Nano was used to detect the Dynamic Light Scattering data of the NPs.

2.3. Bio-TEM

A total of 10^6 cells were planked in 10 cm plates one day ahead of the experiment. The original cell culture used RPMI Medium 1640 (Invitrogen, 11875-093, Waltham, MA, USA) containing 10% FBS (Gibco, Billings, MT, USA), 1% NEAA (Invitrogen 11140050), 1% Gluta-max (Invitrogen 35050061), 1% Sodium Pyruvate 100 mM Solution (Invitrogen 11360070), and 1% penicillin–streptomycin (Sigma, St. Louis, MI, USA). Then, the original cultural medium was replaced with another, containing 10^{-3} M Cys-MoO$_2$ NPs. After another 24 h, the cell samples were harvested for detection via transmission electron microscopy.

2.4. PTT Effect on PTC Cells

Cells were planked at a density of 10^6 cells per 10 cm plate one day in advance; then, the medium was replaced by another containing 10^{-3} Cys-MoO$_2$ for another 24 h. The medium was refreshed to the original one before focusing 808 nm laser radiation at a central position of the plate at 1 W/cm^2 for 20 min.

2.5. Live/Dead Assay

We used a Calcein-AM/PI Staining Kit to visualize the living and dead cells. Final images were captured using an IX71 microscope (Olympus, Shinjuku City, Japan).

2.6. Statistical Analysis

The presented measurements were repeated at least 3 times. One-way ANOVA or a two-tailed independent test was used to analyze differences between groups.

3. Results and Discussion

First, a set of MoO$_{3-x}$ NPs were synthesized by adding varying amounts of cysteine molecules as both reducing and capping agents. As we increased the proportion of cysteine, the resulting solution changed gradually from blue, green, to dark yellow, as shown in Figure 1A. Many studies have proven that the color variation of MoO$_{3-x}$ solutions is due to the degraded valence of the Mo. The Mo valence state of these NP compounds was found to reduce gradually from 2.8 to 2.0 through X-ray surface photoelectron spectrum (XPS) analysis and calculation (Figures 1C,D and S1). It should be noted that the actual specific reduction reaction degree was uncontrollable, with random valence between Mo^{IV} to Mo^{VI} obtained for the mixtures, except for the 80 mg group, which presented a complete Mo reduction. As such, it is difficult to accurately synthesize a specific ratio of cysteine molybdenum oxide, except for MoO$_2$, which can be easily obtained under the condition of sufficient reducing agent and reaction time.

We next compared the light absorption of Cys-MoO$_2$ with that recently reported for Cys-MoO$_{2.8}$, as shown in Figure 1B. It can be seen that the yellow group performed better in the VL region, and also presented a high response in NIR region.
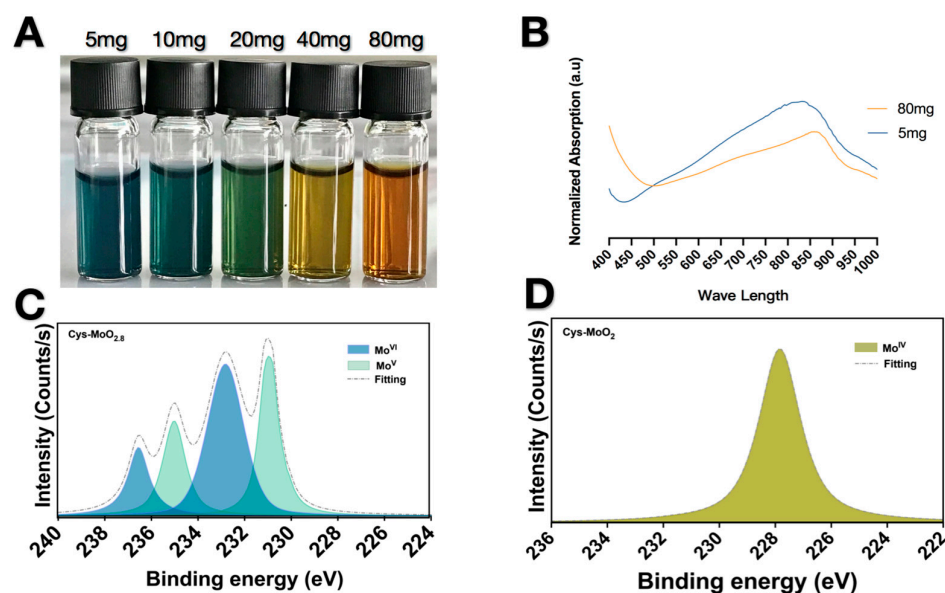
Figure 1. MoO_{3-x} NPs were obtained by adding 5 mg, 10 mg, 20 mg, 40 mg, or 80 mg of cysteine: (**A**) Final solutions present different colors, referring to different Mo valence states; (**B**) UV–vis absorption spectra of Cys-$MoO_{2.8}$ and Cys-MoO_2; (**C,D**) X-ray photoelectron spectroscopy (XPS) measurements of the mild and complete reducing MoO_{3-x} NPs with valence states calculated to be Cys-$MoO_{2.8}$ and Cys-MoO_2, respectively.

The morphology of the two solutions with 5 mg and 80 mg added was found to be approximately spherical when analyzed under TEM, as shown in Figure 2A,B. The diameter of the blue mild-reducing NPs was about 5 nm (Figure 2A), while that of completely reduced Cys-MoO_2 NPs was near 30 nm (Figure 2B). Dynamic Light Scattering of the two nanoparticle solutions revealed that the MoO_{3-x} NPs were wrapped and reduced by cysteine, and their hydrodynamic diameters increased to 294.1 nm and 440.2 nm, respectively, with uniform distribution (Figure 2C,D); meanwhile, MoO_3 with no cysteine presented a DLS size of 268.9 nm (Figure S2).
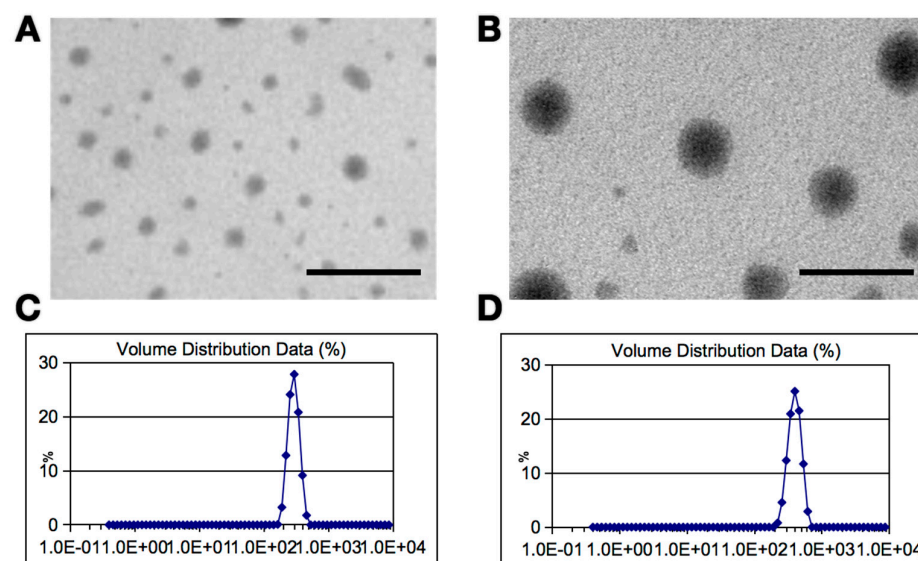

Figure 2. TEM morphology of (**A**): Cys-$MoO_{2.8}$ and (**B**): Cys-MoO_2 NPs. Scale bar: 50 nm. (**C,D**) indicate that the hydrodynamic diameter increased with cysteine coating, being 294.1 nm and 440.2 nm for Cys-$MoO_{2.8}$ and Cys-MoO_2, respectively.

In order to compare the effects of the different concentrations on the essential optical properties of the Cys-MoO$_2$ material, we tested the photoelectric conversion characteristics of the two groups. The NPs were found to adopt a metal–semiconductor–metal structure and, under distinct wavebands and laser irradiation power, we studied the characteristics of the materials with two different concentrations of cysteine as a coating agent. First, Figure 3A,C show the photocurrent curves for the MoO$_{2.8}$ (5 mg) and MoO$_2$ (80 mg) NPs, respectively, in different wavebands. It can be seen, from Figure 3A, that the MoO$_{2.8}$ (5 mg) NPs had the greatest response current in the NIR region (@ 808 nm); meanwhile, from Figure 3C, MoO$_2$ (80 mg) had the highest photocurrent response in visible light (@ 405 nm). This is related to the absorption of the material (Figure 1B). The photocurrent responses at various concentrations were basically consistent with the absorption change and, in this way, changing the concentration of the material can promote the application of the material at different wavelengths. In order to elaborate the properties of materials under differences in external light, we studied the changes in the photocurrent of the MoO$_{2.8}$ (5 mg) and MoO$_2$ (80 mg) NPs by changing the incident power of the laser, as shown in Figure 3B,D. It can be seen, from the figures, that the photocurrents of the NPs with differing concentrations increased linearly with an increase in external incident power, thus proving that both materials have excellent photothermal conversion potential.
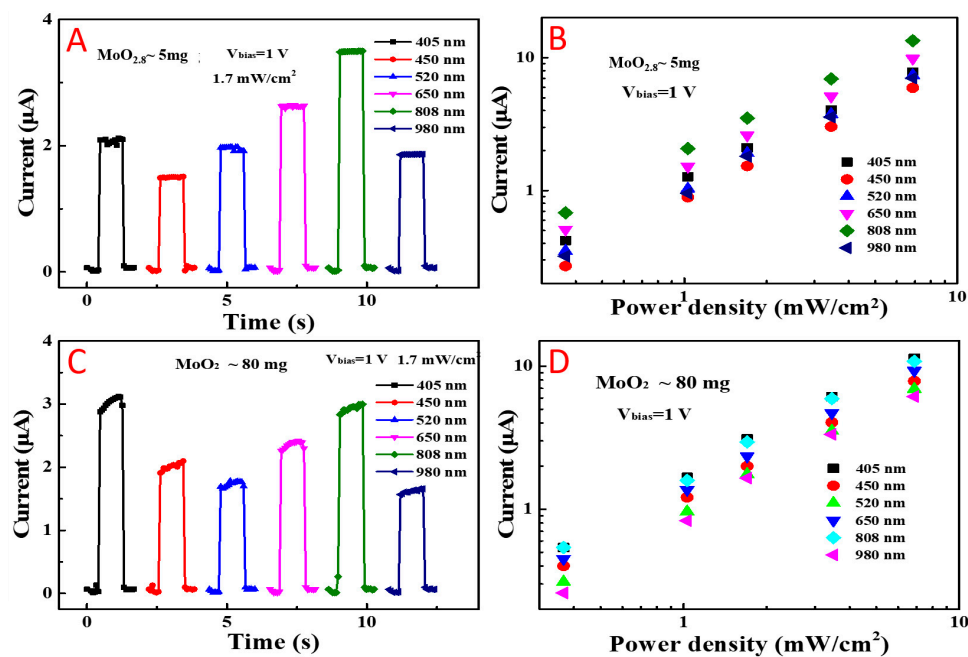

Figure 3. Photoelectronic properties of Cys-MoO$_2$ NPs: (**A,C**). I$_{ph}$ curves of Cys-MoO$_{2.8}$ (5 mg) NPs and Cys-MoO$_2$ (80 mg) NPs with light irradiation at different wavebands (405–980 nm) under 1.7 mW cm^{-2} irradiation power intensity, with V$_{bias}$ = 1 V; (**B,D**). I$_{ph}$ curves of Cys-MoO$_{2.8}$ (5 mg) NPs and Cys-MoO$_2$ (80 mg) NPs under different laser power densities, with V$_{bias}$ = 1 V.

PTT clinical trials typically utilize near-infrared (780–1100 nm) laser photons, due to the well-known relative transparency and capacity of biotissue. With dual photoelectric properties at around 405 nm and 808 nm, the modified Cys-MoO$_2$ presented dramatically improved availability, stability, and optical properties. Therefore, it can be considered an ideal PTA in terms of preparation and synthesis. Furthermore, as it presented special visual light optical properties, we attempted to modify and detect its PTT performance under an 808 nm laser (see Figure S3). Finally, we applied the Cys-MoO$_2$ in an in vitro PTC experiment.

The bio-TEM images in Figure 4A demonstrate the cell endocytosis performance of the Cys-MoO$_2$ NPs. No cellular damage was detected and the cell membrane structure remained uniform without any morphological changes. Figure 4B shows magnified details

on the cellular uptake of the NPs. The Cys-MoO$_2$ NPs clearly gathered into small clusters inside cells and, therefore, are capable of being internalized together.
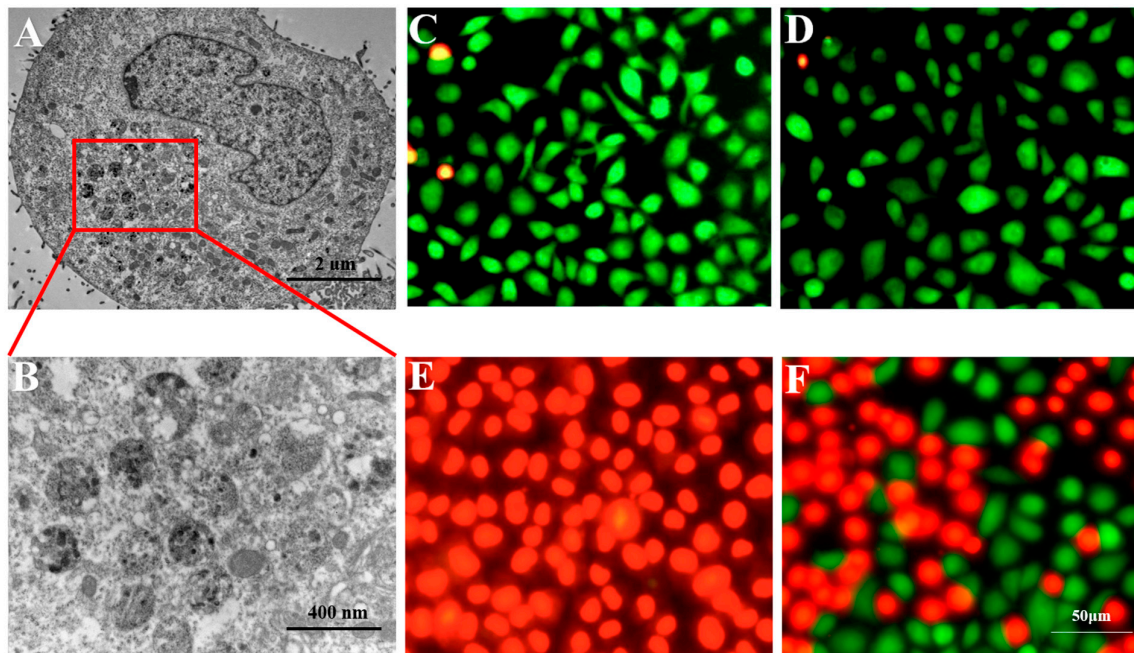

Figure 4. (**A**,**B**): Bio-TEM images showing PTC cell morphology after culturing with Cys-MoO$_2$ NPs for 24 h. Scale bar: (**A**) 2 μm, (**B**) 400 nm. (**C**–**F**): AM/PI staining living cells for green and dead cells for red. (**C**): Group of cells cultured in original medium with only 808 nm laser treatment; (**D**): group of cells cultured with Cys-MoO$_2$ NPs medium but no laser irradiation; (**E**): group of cells cultured with Cys-MoO$_2$ NPs and subjected to 808 nm laser; and (**F**): group of cells cultured with Cys-MoO$_2$ NPs and subjected to 405 nm laser. Scale bar: (**C**–**F**) 50 μm.

After the last medium change, only the NPs inside the cells remained. Then, we began to expose the Cys-MoO$_2$-treated plates to the 808 nm laser. Cell death evidence was imaged via staining: Calcein-AM/PI cells that are dyed green are live cells, while red-stained cells are dead. Neither cells cultured with the mono conditions of 808 nm laser treatment or Cys-MoO$_2$ (Figure 4C and Figure 4D, respectively) showed any statistical difference for the blank control group (Figure S4), with only sparse death signals appearing. In the local irradiation area where the cells died in large quantities, the cell density was lower in the local area irradiated by the laser directly (as shown in Figure 4E), while those in the corner of the well (which is relatively distant) remained alive (as shown in Figure 4F). This phenomenon verifies the calculation results of previous cell activity tests, but also provides visual proof of the PTT effect of Cys-MoO$_2$ NPs on PTC cells. Besides the rinsed dead cells, we counted the proportion of remaining live/dead cells in the irradiated center, which was as low as 1:4. Thus, the inferred cellular activity reached more than 80%, barring those dead cells washed away by PBS. This also indicates that we may easily guarantee the safety of non-objective adjacent normal tissue by controlling the target laser-exposed area when applying Cys-MoO$_2$ NPs in in vivo experiments, or even in clinical use.

Cys-MoO$_2$ presented maximum light–nanomaterial interactions under the 808 nm laser, which is promising for the application of photothermal therapy under a visual laser, which may benefit clinical operations as it helps to balance the efficiency and hyperthermia, while causing lethal and precise damage to PTC cells. PTC cells usually occur in troublesome places (e.g., anatomically adjacent to the arteria carotis or trachea), making relevant surgeries high-risk operations. These specificities regarding the anatomical location of PTCs indicate the promising potential of the application of Cys-MoO$_2$ NPs for local and precise treatment in the clinical treatment of PTC.

To verify the biosafety of the drug, six mice were randomly divided into two groups. The mice were injected with 100 μL normal saline or Cys-MoO$_2$ solution (20 μM) through the tail vein. After 1 week of feeding, the mice were sacrificed for HE tissue staining of vital organs and blood test (as shown in Figure 5), and no obvious abnormalities in the morphology and tissue structure of the heart, liver, spleen, lung, and kidney were observed in the experimental group. Their blood metabolism was also maintained as normal.
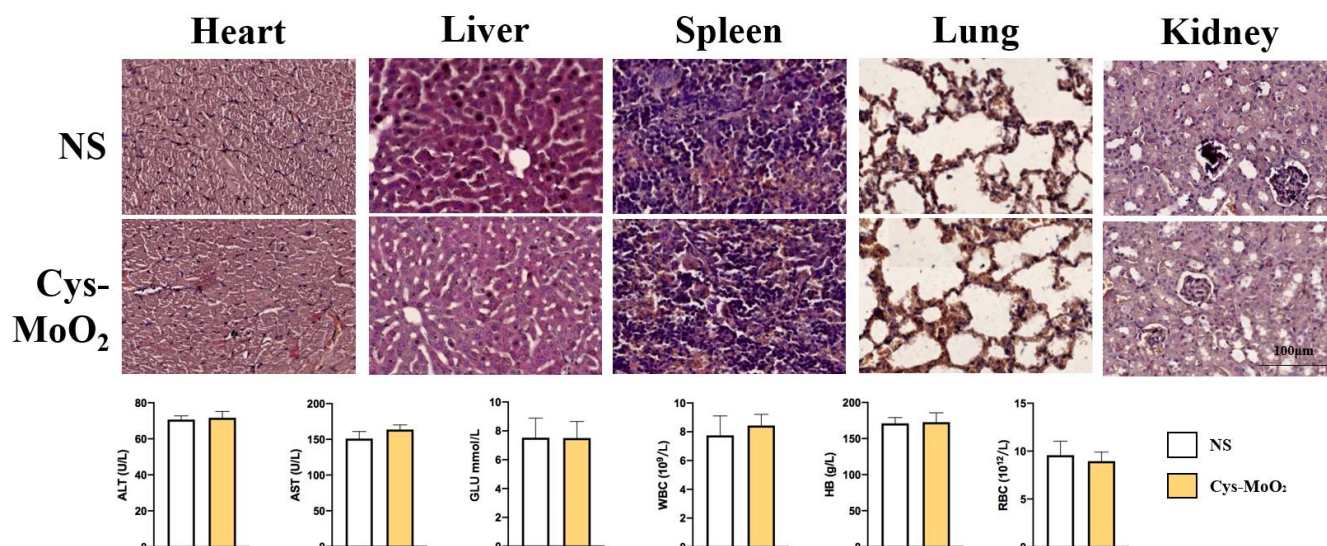

Figure 5. HE staining of heart, liver, spleen, lung, and kidney tissues of mice after caudal intravenous injection of normal saline or Cys-MoO$_2$ photothermal materials. Serum alanine aminotransferase (ALT), aspartate aminotransferase (AST), glucose (Glu), white blood cells (WBC), hemoglobin (HB), and red blood cell (RBC) levels present no significant differences between the two groups.

4. Conclusions

The experimental Cys-MoO$_2$ NPs detailed in this paper provide a solid platform and broad prospect for photothermal therapy against certain cancers. Furthermore, according to existing studies on the synthesis and application of Cys-MoO$_{3-x}$, the reduction in molybdenum oxide by cysteine is affected by many factors, such as the method of addition, frequency, reaction temperature, stirring speed, and so on. We found it difficult to accurately synthesize a specific ratio of cysteine molybdenum oxide, except for MoO$_2$: as long as a sufficient amount of cysteine was added, we successfully obtained the optimized material Cys-MoO$_2$ under mild conditions in a convenient process. Interestingly, this material presented two light absorption peaks: near 405 nm and 808 nm. The wavelength of NIR light in cancer treatment must crucially be considered, as this radiation should satisfy the balance between low off-target interactions and high penetration depth. Treatments using wavelengths higher than 900 nm demand additional precautions when healthy tissues are exposed. The well-advised wavelength 808 nm was found to maximize the light–nanomaterial interactions of Cys-MoO$_2$, guaranteeing selective and effective hyperthermia, and consequently producing irreversible damages to PTCs cells leading to their death by necrosis. Meanwhile, the photothermal conversion efficiency of the Cys-MoO$_2$ NPs in visual wavebands was also notable, which affords the possibility of treating superficial neoplastic lesions through a visual light PTT operation; that is, for superficial lesions, under the condition of a compromised laser penetration, the operation can be visualized and simplified. Further application of multi-point 808 nm laser light and laser irradiation at different wavelengths may enhance the PTT efficiency of Cys-MoO$_2$, allowing for an accurate regulation of the depth of penetration and the targeting region. At the same time, we intend to further explore the drug enrichment ability regarding in vivo application of the developed NPs and the effects of photothermal therapy with their use by means of photoacoustic imaging, survival analysis, and so on, in future experimental works.

PTC tumor tissue has an abnormal vascular system with holes having pore sizes of 20–500 nm. The sizes of the obtained Cys-MoO$_2$ NPs were approximately in this range and, so, we may be able to take advantage of the enhanced permeability and retention effect, as well as the prevention of removal through impaired tumor lymphatic drainage, achieved by passive enrichment in local tumor area. The described PTT agent with VL–NIR region wide-band response has great potential as a phototherapeutic option, satisfying the balance between therapeutic effect and bio-safety, thus opening the door for the application of chiral transition metal oxides with response in the visible light range.

Supplementary Materials: The following supporting information can be downloaded at: https: //www.mdpi.com/article/10.3390/coatings13091552/s1, Figure S1: Typical XPS measurements of Cys-MoO$_{3-x}$; Figure S2: Hydrodynamic diameters of MoO$_3$ solution without cysteine reduction; Figure S3: Temperature versus time curves of Cys-MoO$_2$ under 808 nm radiation; Figure S4: Cell cultured with original medium but no NPs medicine and laser irradiation.

Author Contributions: Validation and writing original draft preparation, J.C.; methodology, X.L.; supervision, X.Z.; conceptualization, M.Y.; formal analysis, L.X. All authors have read and agreed to the published version of the manuscript.

Institutional Review Board Statement: The animal study protocol was approved by Ethics Committee of West China School/Hospital of Stomatology Sichuan University (protocol code: WCHSIRB-D-2022-001, Date 6 January 2022) for studies involving animals.

Informed Consent Statement: Not applicable.

Data Availability Statement: Not applicable.

Conflicts of Interest: The authors declare no conflict of interest.

References

1. Chow, L.Q.M. Head and neck cancer. *N. Engl. J. Med.* **2020**, *382*, 60–72. [CrossRef] [PubMed]
2. Siegel, R.L.; Miller, K.D.; Jemal, A. Cancer statistics 2018. *CA-A Cancer J. Clin.* **2018**, *68*, 7–30. [CrossRef] [PubMed]
3. Cramer, J.D.; Burtness, B.; Le, Q.T.; Ferris, R.L. The changing therapeutic landscape of head and neck cancer. *Nat. Rev. Clin. Oncol.* **2019**, *16*, 669–683. [CrossRef] [PubMed]
4. Vecchia, C.L.; Malvezzi, M.; Bosetti, C. Thyroid cancer mortality and incidence: A global overview. *Int. J. Cancer* **2015**, *136*, 2187–2195. [CrossRef] [PubMed]
5. Wiltshire, J.J.; Drake, T.M.; Uttley, L.; Balasubramanian, S.P. Systematic review of trends in the incidence rates of thyroid cancer. *Thyroid* **2016**, *26*, 1541–1552. [CrossRef]
6. Haugen, B.R.; Alexander, E.K.; Bible, K.C. American Thyroid Association management guidelines for adult patients with thyroid nodules and differentiated thyroid cancer: The American Thyroid Association guidelines task force on thyroid nodules and differentiated thyroid cancer. *Thyroid* **2016**, *26*, 1–133. [CrossRef]
7. Mauri, G.; Gennaro, N.; Lee, M.K. Laser and radiofrequency ablations for benign and malignant thyroid tumors. *Int. J. Hyperth.* **2019**, *36*, 13–20. [CrossRef]
8. Grani, G.; Sponziello, M.; Pecce, V. Contemporary Thyroid Nodule Evaluation and Management. *J. Clin. Endocrinol. Metab.* **2020**, *105*, 2869–2883. [CrossRef]
9. Li, X.; Lovell, J.F.; Yoon, J.; Chen, X. Clinical development and potential of photothermal and photodynamic therapies for cancer. *Nat. Rev. Clin. Oncol.* **2020**, *17*, 657–674. [CrossRef]
10. Huang, D.Y.; Hou, Y.L.; Yang, S.M.; Wang, R.G. Advances in Nanomedicine for Head and Neck Cancer. *Front. Biosci. Landmark* **2014**, *19*, 783–788. [CrossRef]
11. Erin, B.D.; Dreaden, E.C.; Huang, X.; EI-Sayed, I.H.; Chu, H. Gold Nanorod Assisted Near-Infrared Plasmonic Photothermal Therapy (PPTT) of Squamous Cell Carcinoma in Mice. *Cancer Lett.* **2008**, *269*, 57–66.
12. Li, Y.; Lu, W.; Huang, Q.; Huang, M.; Li, C.; Chen, W. Copper sulfide nanoparticles for photothermal ablation of tumor cells. *Nanomedicine* **2010**, *5*, 1161–1171. [CrossRef] [PubMed]
13. Wang, Y.; Meng, H.; Li, Z. Near-infrared inorganic nanomaterial-based nanosystems for photothermal therapy. *Nanoscale* **2021**, *13*, 8751–8772. [CrossRef] [PubMed]

14. Lv, Z.; He, S.; Wang, Y.; Zhu, X. Noble Metal Nanomaterials for NIR-Triggered Photothermal Therapy in Cancer. *Adv. Healthc. Mater.* **2021**, *10*, e2001806. [CrossRef]

15. Huang, X.; Zhang, W.; Guan, G.; Song, G. Design and Functionalization of the NIR-Responsive Photothermal Semiconductor Nanomaterials for Cancer Theranostics. *Acc. Chem. Res.* **2017**, *50*, 2529–2538. [CrossRef]

16. Skrabalak, S.E.; Chen, J.; Au, L.; Lu, X.; Li, X.; Xia, Y. Gold Nanocages for Biomedical Applications. *Adv. Mater.* **2007**, *19*, 3177–3184. [CrossRef] [PubMed]

17. Chen, H.; Shao, L.; Ming, T.; Sun, Z.; Zhao, C.; Yang, B.; Wang, J. Understanding the photothermal conversion efficiency of gold nanocrystals. *Small* **2010**, *6*, 2272–2280. [CrossRef]

18. Yang, K.; Zhang, S.; Zhang, G.; Sun, X.; Lee, S.; Liu, Z. Graphene in mice: Ultrahigh in vivo tumor uptake and efficient photothermal therapy. *Nano Lett.* **2010**, *10*, 3318–3323. [CrossRef]

19. Yang, K.; Feng, L.; Shi, X.; Liu, Z. Nano-graphene in biomedicine: Theranostic applications. *Chem. Soc. Rev.* **2013**, *42*, 530–547. [CrossRef]

20. Sheng, Z.; Hu, D.; Zheng, M.; Zhao, P.; Liu, H.; Gao, D.; Gong, P.; Gao, G.; Zhang, P.; Ma, Y.; et al. Smart Human Serum Albumin-Indocyanine Green Nanoparticles Generated by Programmed Assembly for Dual-Modal Imaging-Guided Cancer Synergistic Photo-therapy. *ACS Nano* **2014**, *8*, 12310–12322. [CrossRef]

21. Yang, K.; Xu, H.; Cheng, L.; Sun, C.; Wang, J.; Liu, Z. In vitro and in vivo near-infrared photothermal therapy of cancer using polypyrrole organic nanoparticles. *Adv. Mater.* **2012**, *24*, 5586–5592. [CrossRef] [PubMed]

22. Hessel, C.M.; Pattani, V.P.; Rasch, M.; Panthani, M.G.; Koo, B.; Tunnell, J.W.; Korgel, B.A. Copper Selenide Nanocrystals for Photothermal Therapy. *Nano Lett.* **2011**, *11*, 2560–2566. [CrossRef]

23. Tian, Q.; Tang, M.; Sun, Y.; Zou, R.; Chen, Z.; Zhu, M.; Yang, S.; Wang, J.; Wang, J.; Hu, J. Hydrophilic Flower-Like CuS Superstructures as an Efficient 980 nm Laser-Driven Photothermal Agent for Ablation of Cancer Cells. *Adv. Mater.* **2011**, *23*, 3542–3547. [CrossRef] [PubMed]

24. Nardine, S.; Abadeer, J.M. Catherine, Recent Progress in Cancer Thermal Therapy Using Gold Nanoparticle. *J. Phys. Chem. C* **2016**, *120*, 4691–4716.

25. Liu, Y.; Pravin, B.; Dai, Z.; Chen, X. Photothermal therapy and photoacoustic imaging via nanotheranostics in fighting cancer. *Chem. Soc. Rev.* **2019**, *48*, 2053–2108. [CrossRef]

26. Høgset, A.; Prasmickaite, L. Photochemical internalisation in drug and gene delivery. *Adv. Drug Deliv. Rev.* **2005**, *56*, 95–115. [CrossRef] [PubMed]

27. Song, G.; Hao, J.; Liang, C.; Liu, T.; Gao, M.; Cheng, L.; Hu, J.; Liu, Z. Degradable Molybdenum Oxide Nanosheets with Rapid Clearance and Efficient Tumor Homing Capabilities as a Therapeutic Nanoplatform. *Angew. Chem. Int. Ed.* **2016**, *55*, 2122–2126. [CrossRef] [PubMed]

28. Zhou, Z.; Wang, X.; Zhang, H.; Huang, H. Activating Layered Metal Oxide Nanomaterials via Structural Engineering as Biodegradable Nanoagents for Photothermal Cancer Therapy. *Small* **2021**, *17*, 2007486. [CrossRef]

29. Shi, J.; Li, J.; Wang, Y.; Cheng, J.; Zhang, C. Recent advances in MoS_2-based photothermal therapy for cancer and infectious disease treatment. *J. Mater. Chem. B* **2020**, *8*, 5793–5807. [CrossRef]

30. Song, G.; Shen, J.; Jiang, F. Hydrophilic molybdenum oxide nanomaterials with controlled morphology and strong plasmonic absorption for photothermal ablation of cancer cells. *ACS Appl. Mater. Interface* **2014**, *6*, 3915–3922. [CrossRef]

31. Li, Y.; Cheng, J.; Liu, Y. Manipulation of Surface Plasmon Resonance in Sub-Stoichiometry Molybdenum Oxide Nanodots through Charge Carrier Control Technique. *J. Phys. Chem. C* **2017**, *121*, 5208–5214. [CrossRef]

32. Zu, H.; Guo, Y.; Yang, H.; Huang, D.; Liu, Z.; Liu, Y.; Hu, C. Rapid room-temperature preparation of MoO_{3-x} quantum dots by ultraviolet irradiation for photothermal treatment and glucose detection. *New J. Chem.* **2018**, *42*, 18533–18540. [CrossRef]

33. Chen, P.; Ma, Y.; Zheng, Z.; Wu, C. Facile syntheses of conjugated polymers for photothermal tumour therapy. *Nat. Commun.* **2019**, *10*, 1192. [CrossRef] [PubMed]

34. Li, Y.; Miao, Z.; Shang, Z.; Cai, Y.; Cheng, J. A Visible- and NIR-Light Responsive Photothermal Therapy Agent by Chirality-Dependent MoO_{3-x} Nanoparticles. *Adv. Funct. Mater.* **2019**, *30*, 1906311. [CrossRef]

35. Xing, Y.; Cai, Y.; Cheng, J. Applications of molybdenum oxide nanomaterials in the synergistic diagnosis and treatment of tumor. *Appl. Nanosci.* **2020**, *10*, 2069–2083. [CrossRef]

36. Zhang, X.; Zhang, J.; Wang, J.; Yang, J.; Chen, J.; Shen, X.; Deng, J.; Deng, D.; Long, W. Highly catalytic nanodots with renal clearance for radiation protection. *ACS Nano* **2016**, *10*, 4511–4519. [CrossRef]

37. Matsumoto, Y.; Nichols, J.; Toh, K.; Nomoto, T. Vascular bursts enhance permeability of tumour blood vessels and improve nanoparticle delivery. *Nat. Nanotechnol.* **2016**, *11*, 533–538. [CrossRef]

38. Bertrand, N.; Wu, J.; Xu, X. Cancer nanotechnology: The impact of passive and active targeting in the era of modern cancer biology. *Adv. Drug Deliv. Rev.* **2014**, *66*, 2–25. [CrossRef]

39. Setyawati, M.I.; Tay, C.Y.; Chia, S.L.; Goh, S.L.; Fang, W. Titanium dioxide nanomaterials cause endothelial cell leakiness by disrupting the homophilic interaction of VE-cadherin. *Nat. Commun.* **2013**, *4*, 1673. [CrossRef] [PubMed]

40. Matsumura, Y.; Maeda, H. A new concept for macromolecular therapeutics in cancer chemotherapy: Mechanism of tumoritropic accumulation of proteins and the antitumor agent smancs. *Cancer Res.* **1986**, *46*, 6387–6392.

41. Chen, J.; Li, Q.; Wang, F.; Yang, M. Biosafety, Nontoxic Nanoparticles for VL–NIR Photothermal Therapy Against Oral Squamous Cell Carcinoma. *ACS Omega* **2021**, *19*, 11240–11247. [CrossRef] [PubMed]